



MWCNTs and Al₂O₃ nanoparticles assembled into silane sol-gel ceramic multi-layer coating to improve surface performance of the magnesium alloy

Maede Sadat Koozegari¹ · Mohammad Reza Tohidifar¹

Received: 7 March 2023 / Accepted: 26 June 2023 / Published online: 3 July 2023

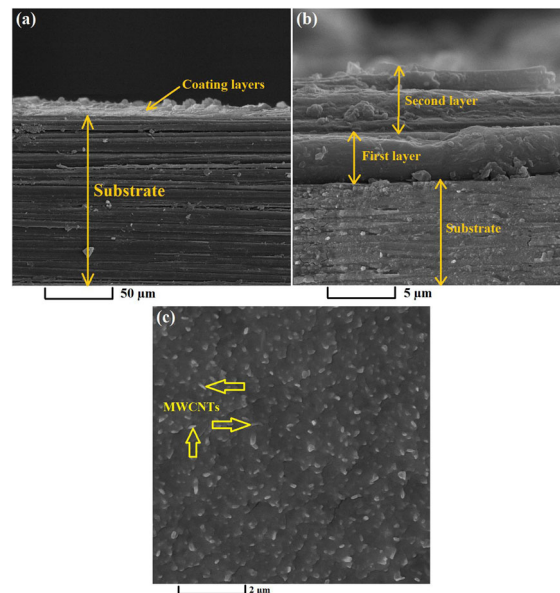
© The Author(s), under exclusive licence to Springer Science+Business Media, LLC, part of Springer Nature 2023

Abstract

This paper reports the successful deposition of mono- and double-layer coatings of silane-Al₂O₃/multi-walled carbon nanotube (MWCNT) nanocomposites on magnesium alloy (AZ91) by sol-gel dip coating technique to improve the corrosion behavior. Scanning electron microscopy, atomic force microscopy, electrochemical impedance spectroscopy, and potentiodynamic polarization techniques were utilized to assess the protective performance of the coatings with various MWCNT contents (0.02, 0.05, 0.1, and 0.15 wt.%) and constant Al₂O₃ concentration (2 wt.%). The incorporation of an optimal amount of MWCNTs (0.1 wt.%) into the mono-layer coating led to corrosion resistance with polarization resistance and roughness of 183.4 kΩcm² and 23.97 nm, respectively. In the case of the double-layer coatings, 0.15 wt.% MWCNT was the optimal value as it significantly increased the polarization resistance (349.6 kΩcm²) and reduced the roughness (5.58 nm), and cracking. The mentioned coating system can be a promising candidate to protect AZ91 magnesium alloy against corrosion.

Graphical Abstract

Image (a) shows the cross-sectional FE-SEM micrograph of the double-layer coating at the magnification of 1000×. Image (b) depicts a region zoomed in image (a) with magnification of 10000×. Image (c) illustrates a coating surface as a zoom in image of (b) with magnification of 25000×.



✉ Mohammad Reza Tohidifar
tohidifar@znu.ac.ir

¹ Department of Materials Science and Engineering, University of Zanjan, P.O. Box 45371-38791, Zanjan, Iran

Keywords Sol-gel · Dip coating · Nanocomposite · Electrochemical impedance spectroscopy · Scanning electron microscopy

Highlights

- Using the 0.1 wt.% MWCNTs into monolayer coating led to improve corrosion behavior.
- Using the 0.15 wt.% MWCNTs into double-layer coating improved the corrosion conduct.
- Roughness of the double-layer coatings was reduced by increasing the MWCNTs.
- Roughness of the mono-layer coatings raised up to 0.1 wt.% followed by a decrement.
- Double layer coating containing 0.15 wt.% MWCNTs could be more protective system.

1 Introduction

As one of the metals with lightest weight, magnesium (with a density of about 1.7–2 g/cm³) and its alloys have been extensively employed in various applications such as transportation and aerospace [1–3]. The series of versatile properties such as lightness and strength has introduced Mg and its alloys as important metals for special applications [4, 5]. AZ91 is the most important magnesium alloy with extensive applications in various industrial products [4, 5]. Despite these excellent advantages, high electrochemical reactivity and poor corrosion resistance of AZ91 have hindered the development of this magnesium alloy [4, 5]. Therefore, the interfacial electrochemical properties should be improved before its application. Coating the surface of magnesium alloys by the sol-gel technique is one of the most effective approaches to prevent corrosion in addition to improving the surface features. The sol-gel method has opened new horizons in a wide range of applications including the coating process. This technique enables the covalent binding between the substrate alloy and the coating with sufficient adhesive strength [4–8]. A fundamental problem with sol-gel derived coatings is their micro/nanoscale porosity and cracked structure as a result of drying and heating processes [9–11]. The cracks can be formed during solvent evaporation, leading to remarkable shrinkage and internal stress, ending up in undesirable porosities in the coating structure. These defects facilitate the penetration of corrosive agents and invasive ions through the pores, promoting substrate corrosion, and declining the anti-corrosion capacity of the coating [9–11].

Several methods have been recently employed to improve the corrosion resistance of the protective sol-gel films. For example, a nano-scale coating with filling properties and unique features has been investigated [12–19]. Based on the results, the incorporation of filler nanomaterials ameliorated the protective behavior of the coating, as the coating defects are filled by the additive nanoparticles, leading to a denser and thicker film [20–24]. In this regard, concentration, dispersion, and exfoliation of the nanoparticles are the key factors. [20–24].

Carbon nanotubes (CNTs) are a class of carbon-based nanomaterials with extensive applications as novel reinforcement filler for the composite coatings due to their outstanding properties such as good strength and electronic conductivity, light weight, mechanical and thermal durability, specific nano-scale tubular characteristics, corrosion resistance, hydrophobicity, and large specific surface area [25–27]. CNT-containing hybrid materials (especially, nanocomposites coatings) have gained increasing popularity due to their interesting characteristics which can mechanically, electrically, thermally, and electrochemically improve the final coating [25–27].

However, the influence of the CNTs on the corrosion behavior of the coatings of magnesium alloys prepared by sol-gel technique has rarely been studied. Seifzadeh et al. [28] dispersed the MWCNTs in phenyl-trimethoxy silane sol and deposited the resultant sol-gel nanocomposite on AM60B magnesium alloy. They reported a remarkable enhancement in the corrosion capacity of the PTMS sol-gel coating after loading appropriate amount of MWCNTs due to the formation of more compact coating with lower porosity [28]. Lopez et al. [29] addressed the MWCNTs-reinforced sol-gel silica coatings deposited on magnesium alloy and reported the homogeneous and dense composite coatings. In other research work, Fernandez et al. reported silicon oxide multilayer coatings doped with carbon nanotubes and graphene nanoplatelets to protect magnesium alloy against corrosion [30]. They reported significant improvement in the corrosion behavior through the formation of a compact and homogeneous coating [30]. Moreover, Daavari et al. [31] investigated the corrosion behavior of AZ31B magnesium alloy with hybrid MWCNTs-PEO/PCL coatings and found that the incorporation of MWCNTs induced several structural and functional modifications in the PEO coatings.

A summary of the reviewed articles indicated that the presence of a material with filler characteristics beside the MWCNTs can effectively fill the pores, forming a denser coating on the magnesium alloy. Alumina (Al₂O₃) nanopowder is a filler ceramic material with promising compressive strength, abrasive resistance, chemical durability,

heat conductivity, and thermal shock resistance [32]. This material enjoys more attractive attributes due to its availability as well as cost-effectiveness. Thanks to their filling function, uniformly distributed Al_2O_3 nanoparticles can enhance the wear resistance of the coating while reinforcing the nanocomposite [32].

In this regard, the current research is an attempt to propose a novel coating system to protect the magnesium alloy (AZ91) against corrosion. To this end, Al_2O_3 particles were used as the filler and assembled into a silane composite coating with MWCNTs additive to improve the coating performance. Furthermore, the role and optimal content of MWCNTs in the protection behavior and potential anti-corrosion feature of the coating were assessed in the presence of Al_2O_3 .

2 Experimental procedure

2.1 Chemicals and substrate

Dip-coating of MWCNT/SiO₂ + Al_2O_3 nanocomposite through a sol-gel technique involved the application of different chemicals including reagent grade tetraethyl orthosilicate (TEOS; purity $\geq 99\%$), aluminum oxide (Al_2O_3 ; purity $\geq 99\%$), and sodium dodecyl sulfate (SDS; extra pure). Fine powdered crystals of Al_2O_3 with a density of 3.95 g/cm^3 and mean particle size of $0.1 \mu\text{m}$ were used. Ethyl alcohol (purity $\geq 99.9\%$) and nitric acid (purity $\geq 65\%$) were utilized as chemical solvent and pH-adjusting agent of the sol, respectively. All the mentioned chemicals were purchased from Merck Corporation (Merck KGaA,

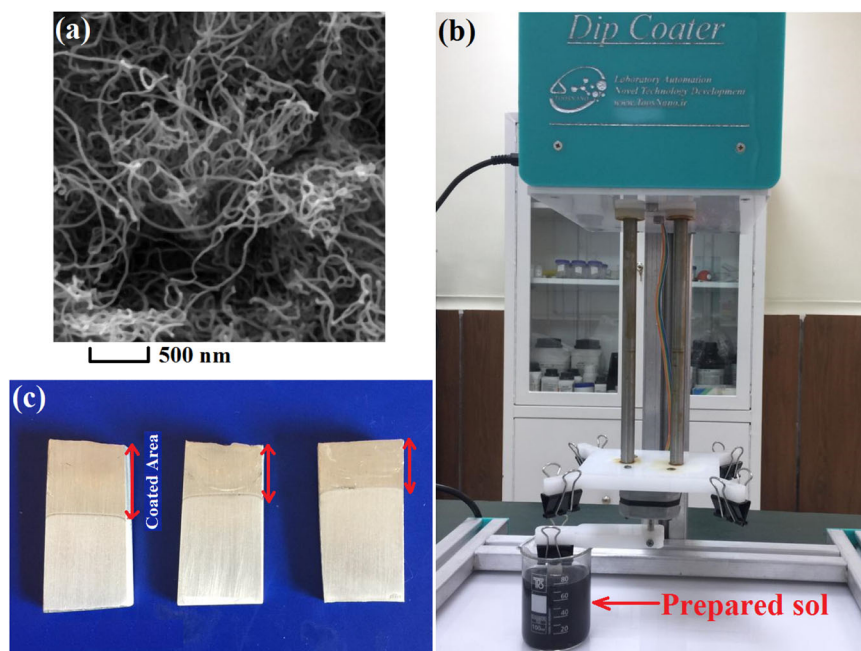
Darmstadt, Germany). Moreover, COOH-functionalized MWCNTs (density of 2.1 g/cm^3 , purity $\geq 98\%$, US Research Nanomaterials; USA) were employed as filler additive. The morphology and structure of the applied MWCNTs were assessed by SEM as depicted in Fig. 1(a). Accordingly, the purchased MWCNTs had an external diameter of 20–30 nm, an internal diameter of 5–10 nm, and a length of 10–30 μm .

AZ91 magnesium alloy composed of 9 wt.% aluminum, 1 wt.% zinc, and 90 wt.% magnesium (base metal) was taken as the substrate. The magnesium alloy bar was sliced by a wire-cut machine into dimensions of $20 \times 10 \times 2 \text{ mm}^3$. The sliced samples were then ground with abrasive papers from 600 to 1000 grits followed by washing with distilled water. An ultrasonic cleaner was also employed to degrease the samples in an ethanol medium at $40 \text{ }^\circ\text{C}$ for 15 min. The samples were washed with distilled water and finally dried by hot air.

2.2 Sol-gel preparation and coating

In a typical procedure, different amounts of MWCNTs (0.02, 0.05, 0.1, and 0.15 wt.%) and a fixed content of Al_2O_3 (2 wt.%) were first dispersed in a mixture of ethyl alcohol and TEOS. SDS (0.6 wt.%) was then added to the system as a surfactant to prevent the aggregation of MWCNTs. The acquired mixture was stirred at 700 rpm for 20 min followed by 45 min of ultrasonication at room temperature and a power of 200 W. At the same time, a specific quantity of acidic water (nitric acid solution with a pH of 1) was added to the system to accelerate the hydrolysis where the molar ratio of TEOS: ethanol: acidic water

Fig. 1 **a** SEM image of the MWCNTs used in the preparation of the nanocomposite coatings; **b** the dip-coating process using the prepared sol, and **c** the coated samples



was maintained at 4:4:1. The mixture was further stirred at 700 rpm for 4 h and again ultrasonicated for about 1 h at room temperature. The resulted sol was transferred into a glass container covered by aluminum foil and kept at room temperature for 48 h to be used in the coating process.

Three different coating systems were deposited on the magnesium alloy: (1) Simple SiO₂ coating (with no MWCNTs and Al₂O₃) derived from silica sol to evaluate the effect of MWCNTs and Al₂O₃ on coatings performance, (2) mono-layer coating of MWCNT/SiO₂ + Al₂O₃ with different MWCNT contents (2 wt.% Al₂O₃), and (3) double-layer coatings to investigate the effect of coating layers number on corrosion resistance at the presence of different MWCNT concentrations whose first layer includes MWCNT/SiO₂ (with no Al₂O₃) and the second layer consists of MWCNT/SiO₂ + Al₂O₃ (2 wt.%); both layers had equal MWCNT contents.

Dip-coating technique was employed to deposit the nanocomposite on the magnesium alloy. For this purpose, the sliced samples were vertically dipped into the synthesized sol using a dip-coater (Toos Nano Equipment, Iran). The specimens were kept in the solution for 3 min and then withdrawn at a constant rate of 12 cm/min. Figure 1(b) illustrates the dip-coating process while the coated samples are presented in Fig. 1(c). To prevent unwanted defects, the samples were perched in the saturated medium of ethanol for 24 h to control the water and alcohol evaporation rate. The coated samples were then transferred to an oven and heated at 60 °C for 1 h followed by further heat treatment at 130 °C for a soaking time of 2 h to accomplish the condensation process under the heating rate of 1 °C/min. A similar rate was applied to cool the specimens in the oven.

2.3 Characterization methods

The microstructure and surface morphology of the samples were investigated using a scanning electron microscope (TESCAN FE-SEM MIRAI) equipped with an energy dispersive X-ray spectroscope (EDS). Given the insulating behavior of the coatings, they were coated with gold prior to the SEM analysis to resolve the surface charge aggregation.

The surface roughness of the mono- and double-layer coatings was examined on a scanning scale of 3 × 3 μm² using an Atomic Force Microscope (AFM, Veeco CP II).

The interfacial electrochemical properties of the specimens, their corrosion resistance, and corrosion rate were evaluated at different immersion times through the electrochemical impedance spectroscopy (EIS) and potentiodynamic polarization (PD) tests. Impedance spectra and PD curves were recorded using a computer-controlled Origa-flex potentiostat/galvanostat apparatus supported by Origa-Master 5 software. EIS and PD analyses were performed in a corrosive solution containing 3.5 wt.% NaCl at room

temperature (25 °C) using a classic three-electrode electrochemical cell. The coated samples were considered as the working electrode and covered with lacquer to maintain an exposed area of 1 cm². The applied electrochemical cell encompassed three electrodes including a platinum sheet with an area of 1 cm², a reference Ag-AgCl (3 M KCl) electrode, and the working electrode. To record the impedance response of the specimens, an AC perturbing voltage signal with an amplitude of 10 mV was applied within a frequency range of 10 kHz to 100 mHz. Impedance responses were acquired as various plots through the corrosion potential in 200 mL of the corrosive solution of NaCl for different exposure times. Potentiodynamic polarization measurements were recorded as supplementary tests after immersing in a corrosive solution for 2 h, from −250 mV to +250 mV against the open circuit potential (OCP) by applying the scan rate of 1 mV/S toward the anodic direction.

Phase structures of the various samples were analyzed by X-ray diffraction (XRD, Bruker D8 Advance, Germany) using Cu Kα radiation (λ = 1.54056 Å) with 2 Theta scan range of 5–80° and step size of 0.1 °S^{−1}.

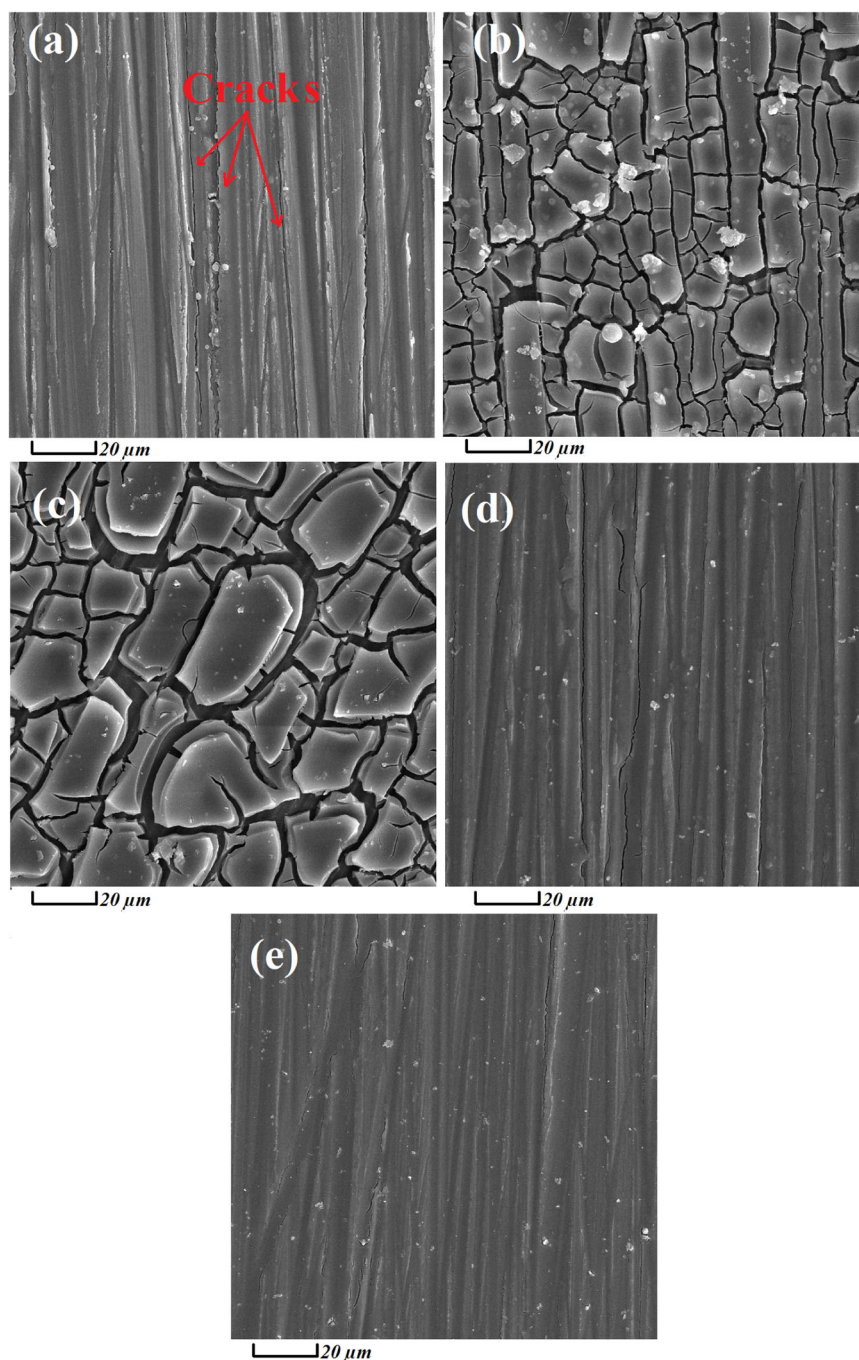
Fourier-transform infrared spectroscopy (FTIR) was carried out to consider the bonding states of coating using a Nicolet Nexus 6700 apparatus in the wavenumber range of 400 to 4000 cm^{−1}.

3 Results and discussion

3.1 SEM observations

Fig. 2(a) shows the FE-SEM micrograph of pristine SiO₂ coating free of MWCNTs and Al₂O₃. Figure 2(b–e) depict the FE-SEM micrographs of double-layer coatings whose first layer contain different MWCNTs contents (0.02, 0.05, 0.1, and 0.15 wt.%) with no Al₂O₃ whereas their second layer contains 2 wt.% Al₂O₃ along with different MWCNT concentrations. Meanwhile, the MWCNT content of both layers was the same. As seen, some cracks were formed in the coating free of MWCNTs and Al₂O₃ (Fig. 2(a)). Moreover, the cracks show an increase in the specimens containing 0.02 and 0.05 wt.% MWCNTs in comparison with Fig. 2(a). However, the coatings containing 0.1 and 0.15 wt.% MWCNTs (Fig. 2(d, e)) exhibited lower cracking. Despite the lower cracks in the coatings containing 0.15 wt.% MWCNTs compared to the one with 0.1 wt.% MWCNTs, its cracks are also at a minimum level in comparison with Fig. 2(a). This trend confirmed the reduction of cracks through an increase in MWCNT concentration. The reduced number of cracks in the coating can be assigned to the thermal conductivity of MWCNTs [28], as the so-called thermal shock is the main source of coating cracks during

Fig. 2 SEM micrographs of (a) the pristine coating with no MWCNTs and Al_2O_3 and double-layer coatings with (b) 0.02 wt.%, (c) 0.05 wt.%, (d) 0.1 wt.%, and (e) 0.15 wt. MWCNTs along with 2 wt.% Al_2O_3

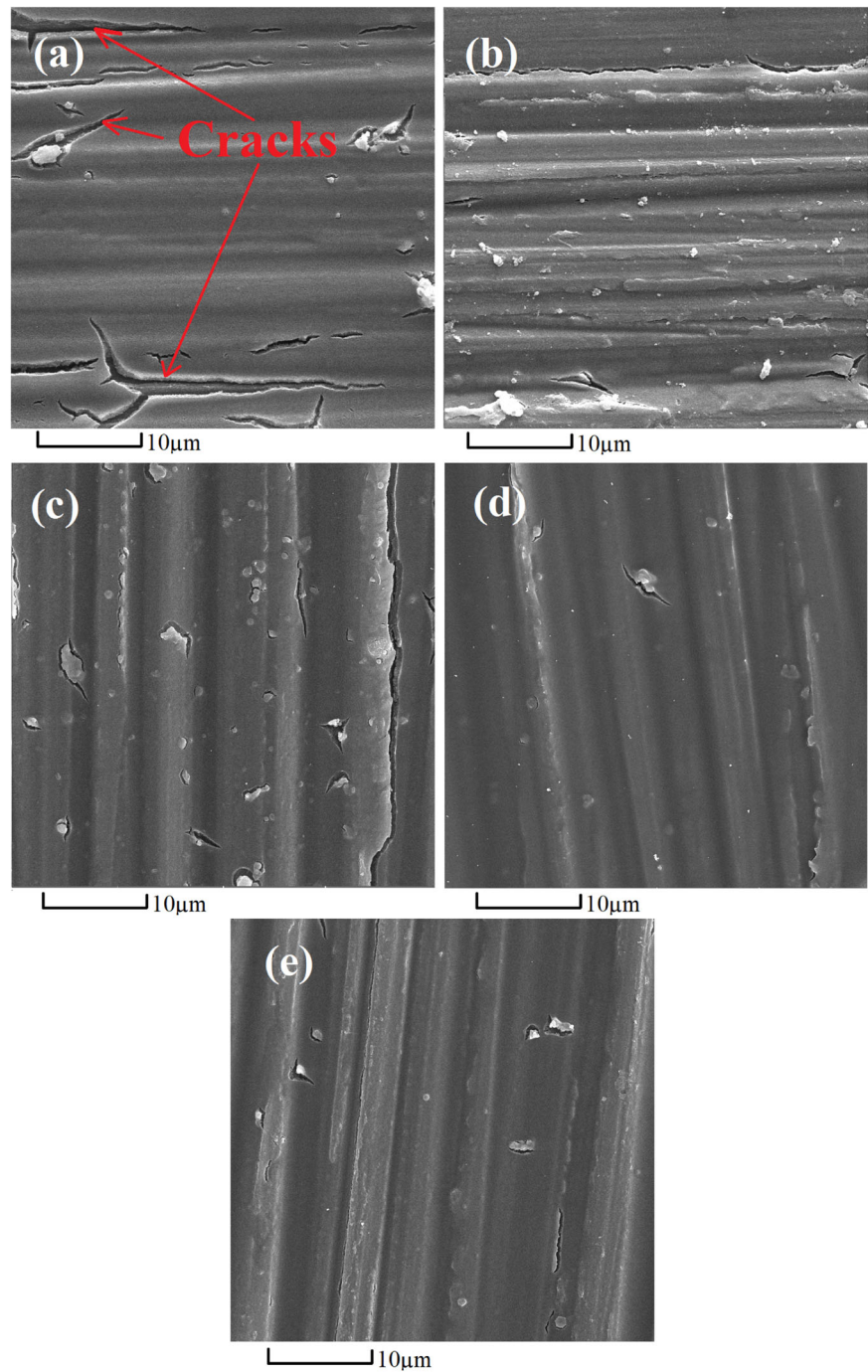


the drying and heating stages. Thermal shock resistance of the coating system with adequate MWCNTs will be considerable due to the higher thermal conductivity of MWCNTs. At lower MWCNT contents, however, the thermal shock resistant mechanism cannot be activated due to insufficient MWCNTs content; therefore, the coating components (MWCNTs and Al_2O_3 particles) could not sufficiently fill the spaces between the developed cracks, resulting in a cracked coating. In contrast, an increase in thermal conductivity contributes to the improvement of

thermal shock resistance at higher MWCNT concentrations. Additionally, the reinforcing role of MWCNTs in nanocomposite coating can also prevent the nucleation and propagation of cracks at high MWCNT contents (0.15 wt.%) while this phenomenon is negligible at lower MWCNT levels.

Fig. 3(a) shows the FE-SEM micrograph of pristine silane coating with no MWCNTs and Al_2O_3 . Several cracks can be observed on the coating surface that can be created during the drying and heating stages. Figure 3(b–e) shows

Fig. 3 The SEM micrographs of (a) the pristine coating and the mono-layer coatings with (b) 0.02 wt.%, (c) 0.05 wt.%, (d) 0.1 wt.%, and (e) 0.15 wt.% MWCNTs along with 2 wt.% Al_2O_3



the FE-SEM micrographs of mono-layer nanocomposite coating containing various contents of MWCNTs and a fixed amount of Al_2O_3 (2 wt.%). As can be seen, the cracks increased in the coatings containing 0.02 and 0.05 wt.% MWCNTs (Fig. 3(b, c)) as compare to Fig. 3(a). It seems that at lower contents of MWCNTs (<0.1 wt.%), inadequate filling of the inter-crack spaces facilitates the crack propagation. In other words, the poor filling performance of the coating components due to lower nanotube concentrations outshone the improving role of MWCNTs in the thermal

shock resistance of nanocomposite under the mentioned conditions. Figure 3(d) depicts a significant decline in the size and number of the cracks in the coating containing 0.1 wt.% MWCNTs. The reinforcing impact of MWCNTs along with its superior thermal conductivity seemed to more effectively reduce the defects as the coating with 0.1 wt.% MWCNTs exhibited minimum cracking. On the other hand, cracks increased in the nanocomposite loaded with 0.15 wt.% MWCNTs (Fig. 3(e)). In such cases (MWCNT loading >0.1 wt.%), aggregation of MWCNTs probably

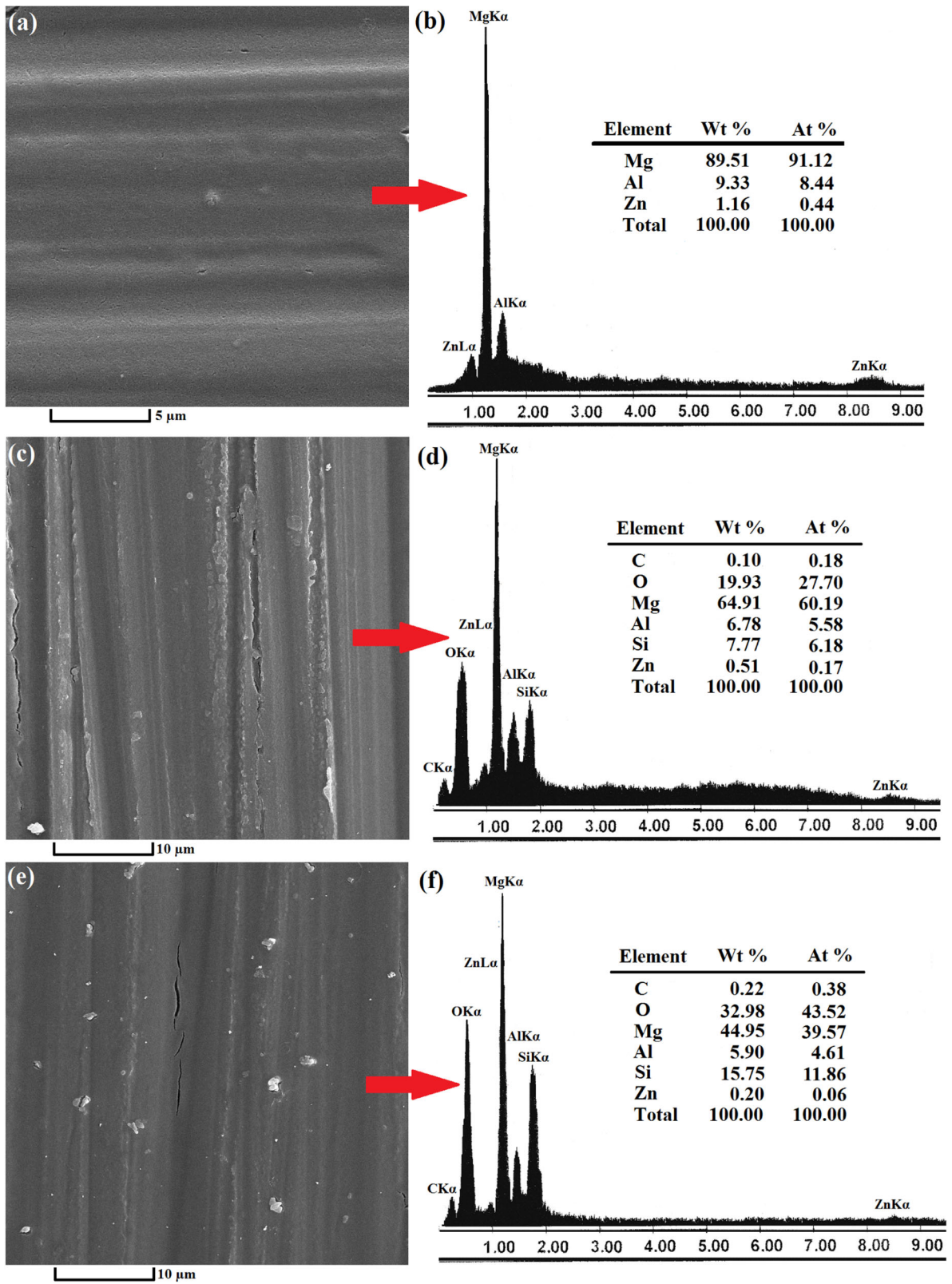


Fig. 4 The SEM micrographs and their corresponding EDS results of (a, b) pristine AZ91 Mg alloy, (c, d) mono-layer, and (e, f) double layer coatings of SiO₂ + Al₂O₃/MWCNT nanocomposite

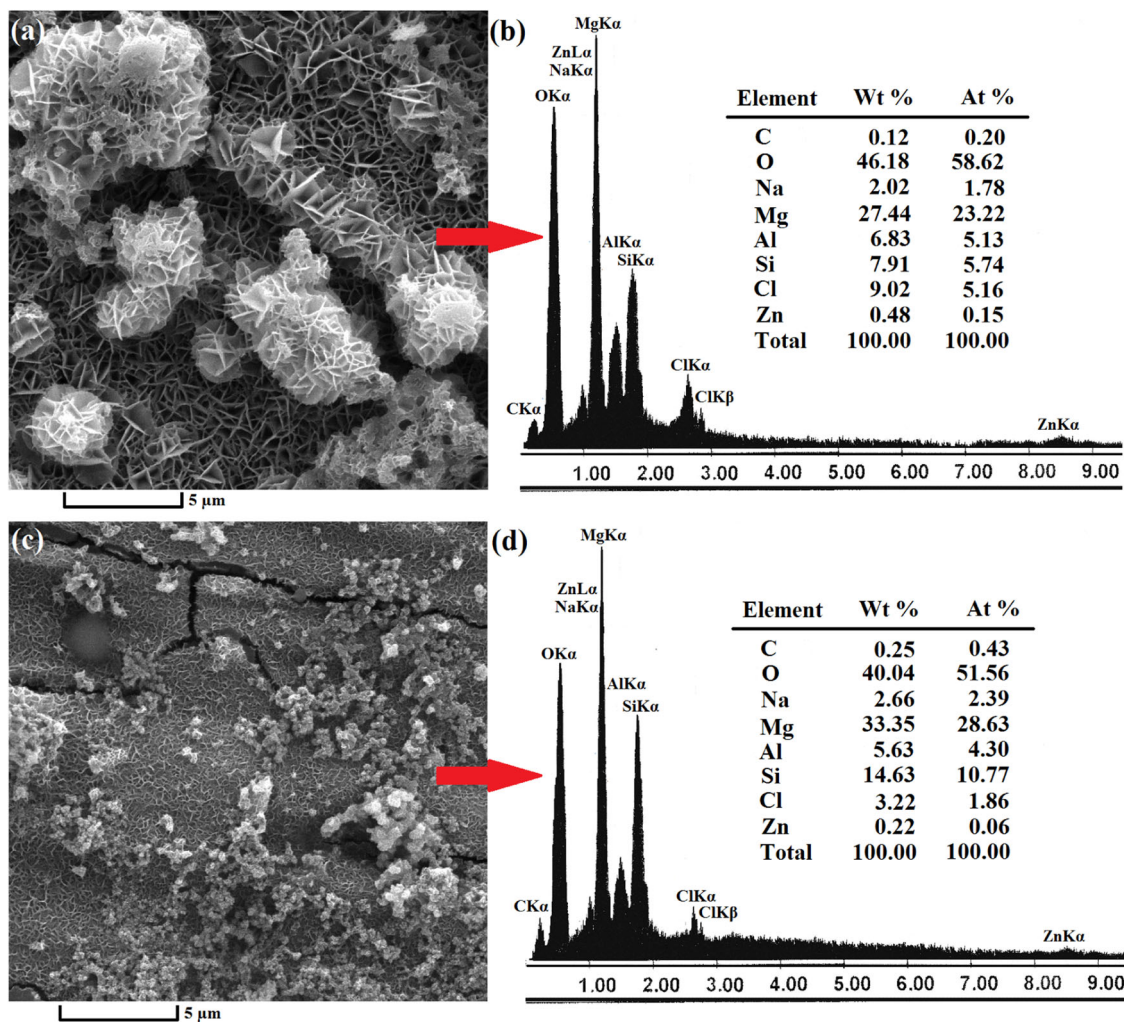


Fig. 5 The SEM micrographs of corroded samples after immersing in 3.5% NaCl solution for 480 min along with their corresponding EDS results: (a, b) mono-layer, and (c, d) double-layer coatings of $\text{SiO}_2 + \text{Al}_2\text{O}_3/\text{MWCNT}$

leads to the heterogeneous and non-uniform distribution of MWCNTs in the coating matrix, forming cracking channels. Furthermore, the optimal MWCNTs content for mono-layer coating was assessed to be about 0.1 wt.%.

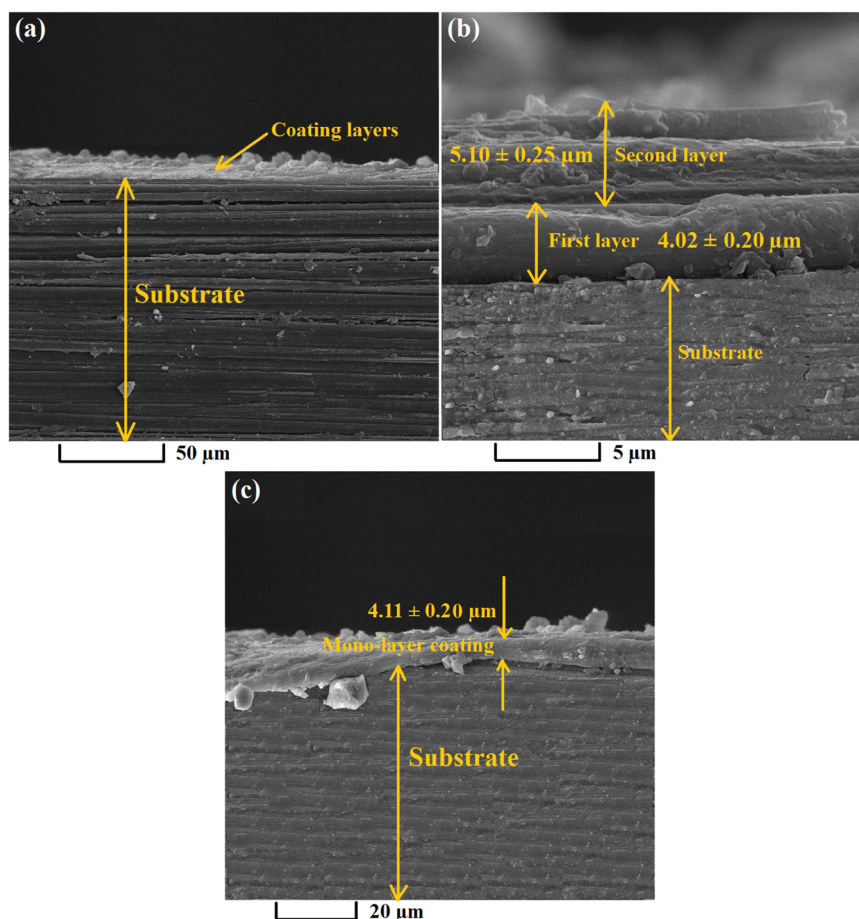
Fig. 4 shows the FE-SEM micrographs and corresponding EDS results of pristine AZ91 magnesium alloy as well as mono- and double-layer coatings. As can be observed, the concentration of coating constituents increased in the coated samples; while the base and main alloying elements showed a decrease, confirming their deposition on the alloy surface. Based on Fig. 4(e, f), double-layer coating possesses higher and lower concentrations of coating and base elements, respectively showing a higher thickness of the coating.

Fig. 5 shows the FE-SEM micrographs of the corroded samples (mono- and double-layer coating) after the EIS tests (immersion in 3.5% NaCl solution for 480 min) along with their corresponding EDS results. The micrographs revealed

the lower corrosion of double-layer coating (Fig. 5(c, d)) compared to other samples. Additionally, large quantities of oxygen and chlorine were detected in EDS diagrams, indicating the formation of the corrosion layer. However, mono-layer coating showed higher corrosion products compared to the double-layer coatings, suggesting the proper corrosion resistance of the double-layer coating.

The detailed structures of the interface between AZ91 and composite coatings of the mono- and double-layer samples as the cross-sectional FE-SEM images can be found in Fig. 6. Accordingly, the thickness of the mono-layer and double-layer coatings was 4.11 ± 0.20 and 5.10 ± 0.25 μm , respectively. The difference in the thickness of the first and second layers can be due to the different substrate characteristics where high deposition can be achieved on ceramic substrate ($\text{SiO}_2/\text{MWCNT}$) against the AZ91 magnesium alloy at constant dipping time. As observed, an appropriate physical contact surface between

Fig. 6 Cross-sectional SEM images of $\text{SiO}_2 + \text{Al}_2\text{O}_3/\text{MWCNT}$ nanocomposite containing 0.15 wt.% MWCNTs: (a) double-layer coating with low magnification, (b) double-layer coating with high magnification, and (c) mono-layer coating with high magnification



AZ91 and composite coatings was formed; a proper protective performance can be consequently expected.

The microstructure evolution of the composite coatings is presented in Fig. 7 at various conditions including as-synthesized, dried, heat-treated, and corroded (after immersing in 3.5% NaCl solution for 480 min). Accordingly, as-synthesized coating showed a crack-free microstructure (Fig. 7(a)), while the dried sample offered a cracked structure in which filler particles were distributed within the spaces between the cracks (Fig. 7(b)). However, some cracks can be observed in the heat-treated coating which can be minimized under optimal conditions (Fig. 7(c)). Figure 7(d) depicts the corroded structure of the coating along with corrosion products and residual NaCl after 480 min of exposure to 3.5% NaCl solution.

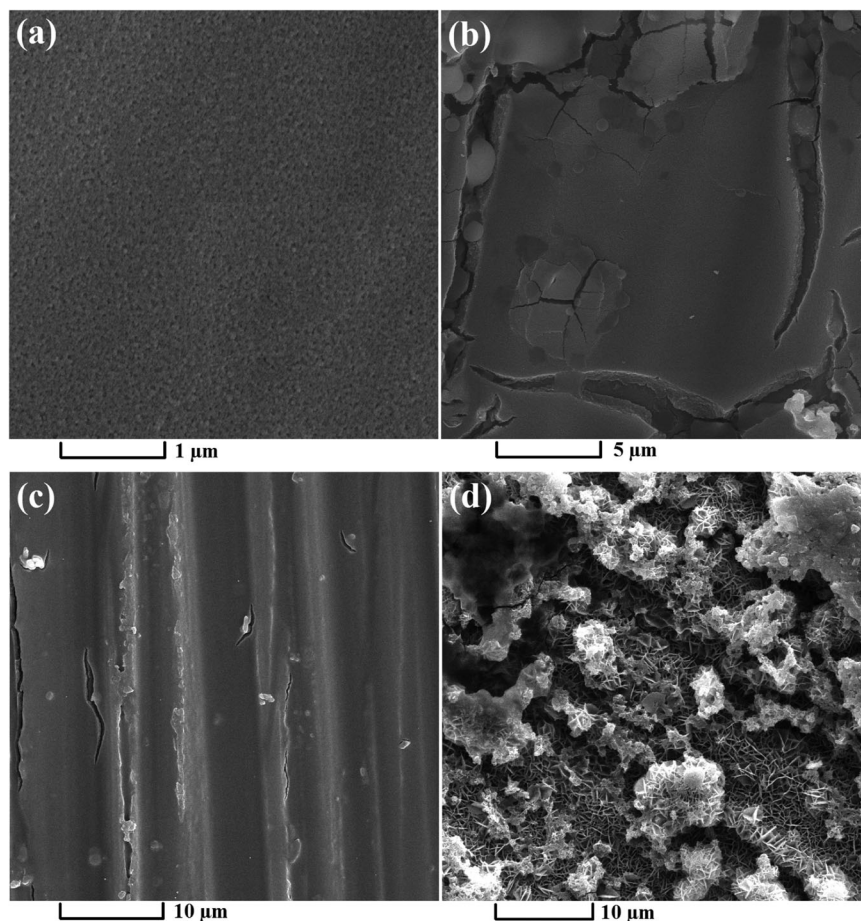
Fig. 8 illustrates the MWCNTs distributed in the fabricated samples including surface of double-layer coating (a), $\text{SiO}_2/\text{MWCNT}$ and $\text{SiO}_2 + \text{Al}_2\text{O}_3/\text{MWCNT}$ nanocomposites (without substrate) (b, c), and surface of double-layer coating after subjecting the EIS analysis for 480 min (0.15 wt.% MWCNT). As can be seen, Fig. 8(a) shows the fibrous morphology of MWCNTs in the coating. This figure also confirms the tight interface bonding between the MWCNTs and silane matrix of the coating and the proper distribution

of carbon nanotubes in the coating structure. Fig. 8(b, c) also confirm the uniform distribution of MWCNTs in the silane matrix nanocomposites after the heat treatment. Figure 8(d) exhibits the distribution of MWCNTs on the surface of corroded coating in which MWCNTs still remained in the coating structure after EIS test.

3.2 AFM studies

Fig. 9 shows the topographic AFM images of simple and double-layer nanocomposite coatings. The average roughness (R_a) of the pristine coating (free of MWCNTs and Al_2O_3) (Fig. 9(a)) was 68.74 nm which rose to 86.81 nm in the double-layer coating containing 0.02 wt.% MWCNTs. Such an increment in the roughness could be attributed to the presence of nanostructured MWCNTs and Al_2O_3 particles. Some studies [29–33] have reported the enhancement of surface roughness upon the insertion of nanoscale constituents into the sol-gel coating. The R_a values of the coatings containing 0.05, 0.1, and 0.15 wt.% MWCNTs were 23.54, 8.06, and 5.58 nm, respectively. An increase in MWCNT concentration declined the surface roughness of the coating. Noteworthy, MWCNTs along with Al_2O_3 particles could be distributed within the spaces between the

Fig. 7 The microstructure evolution of the composite coatings at various conditions: (a) as-synthesized, (b) dried, (c) heat-treated, and (d) corroded (after immersing in 3.5% NaCl solution for 480 min) samples



developed cracks, leading to a dense and thick coating with less porosity and lower roughness.

Fig. 10 shows the 3D AFM micrographs of simple and mono-layer $\text{SiO}_2 + \text{Al}_2\text{O}_3/\text{MWCNT}$ nanocomposite coatings containing different MWCNT contents and constant Al_2O_3 concentration (2 wt.%). Accordingly, the average roughness of the coating with no MWCNTs and Al_2O_3 was 68.74 nm which decreased to 10.92 nm for the mono-layer coating containing 0.02 wt.% MWCNTs. The cracking spaces of the coating are probably filled by MWCNTs and Al_2O_3 particles which decremented the surface roughness. The R_a value rose to 12.76 nm in the coating containing 0.05 wt.% MWCNTs. It appears that the MWCNT content of 0.05 wt.% exceeds the appropriate amounts for filling the crack spaces as it enhanced the roughness. The surface roughness of the coating with 0.1 wt.% MWCNTs was 23.97 nm; while the sample loaded with 0.15 wt.% MWCNTs exhibited a roughness of 6.28 nm. According to Fig. 3, the coating loaded with 0.1 wt.% MWCNTs showed lower cracking. Low MWCNTs contents and Al_2O_3 particles can be placed within the crack spaces, resulting in a significant increase in the surface roughness of the coatings. On the other hand, the coating with 0.15 wt.% MWCNTs exhibited very low roughness possibly due to a sharp

increase in surface cracking such that all MWCNTs and Al_2O_3 particles could be distributed within the cracks space.

3.3 EIS and PD analyses

EIS plots of the pristine coating, as well as double-layer coatings containing 0.02, 0.05, and 0.1 wt.% MWCNTs along with 2 wt.% Al_2O_3 particles, are represented in Supplementary Figs. S1–S4, respectively. The impedance responses of each coated sample are presented in three types of plots: (a) Nyquist, (b) Bode modulus, and (c) phase Bode. The impedance response shows two capacitive semicircles at high and medium frequencies. The time constant emerging at high-frequencies corresponds to the capacitance and resistance of the coating; while the time constant in intermediate frequencies is related to the double layer capacitance and charge transfer resistance [28, 33].

EIS plots of the double-layer coating containing 0.15 wt.% MWCNTs is shown in Supplementary Fig. S5. Two capacitive time constants relative to Nyquist plots correspond to the circuit also illustrated in S5(d). The acquired parameters were extracted by the Zsim software as listed in Supplementary Material (Table S1) according to

Fig. 8 The MWCNTs distributed in the fabricated nanocomposites containing 0.15 wt.% MWCNT: (a) surface of double-layer coating, (b) SiO₂/MWCNT (without substrate), (c) SiO₂ + Al₂O₃/MWCNT (without substrate), and (d) surface of double-layer coating after subjecting the EIS analysis for 480 min

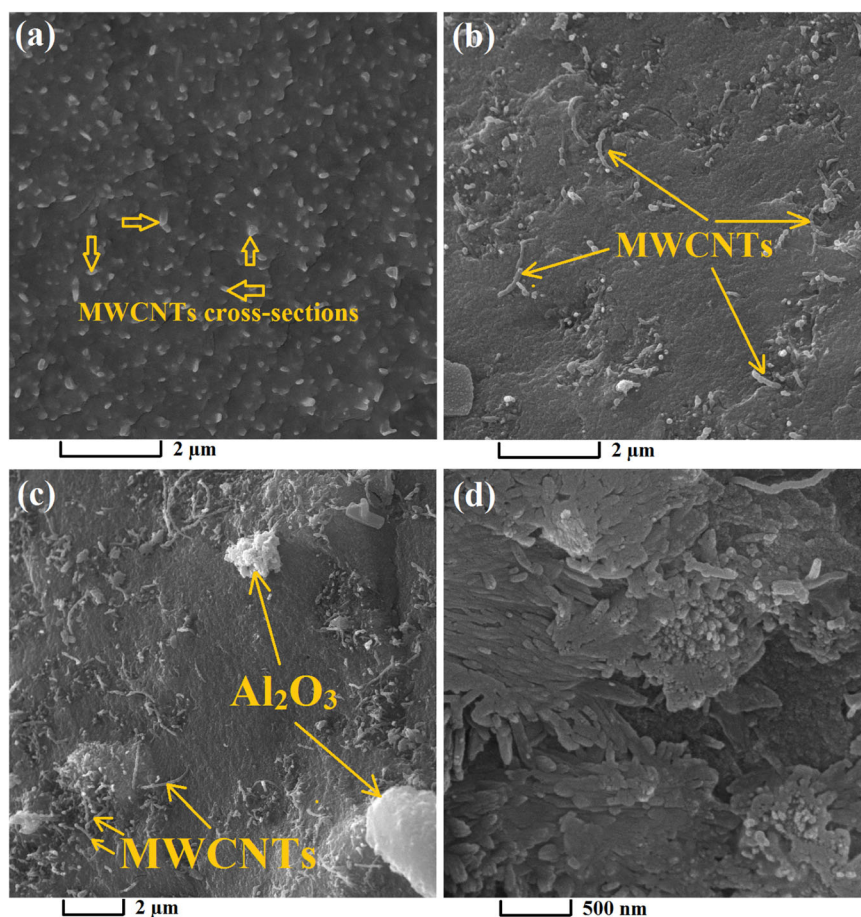
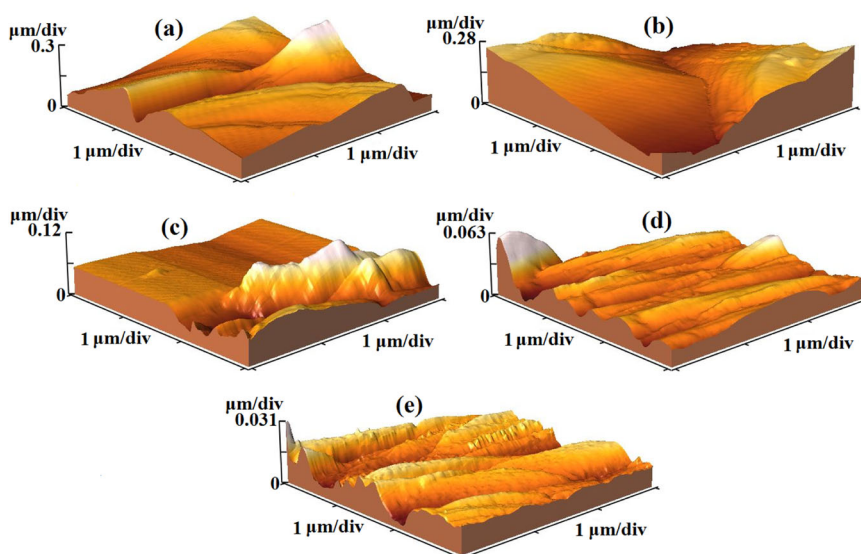


Fig. 9 Topographic AFM images of (a) the pristine coating and double-layer coatings containing (b) 0.02 wt.%, (c) 0.05 wt.%, (d) 0.1 wt.%, and (e) 0.15 wt.% MWCNTs along with 2 wt.% Al₂O₃

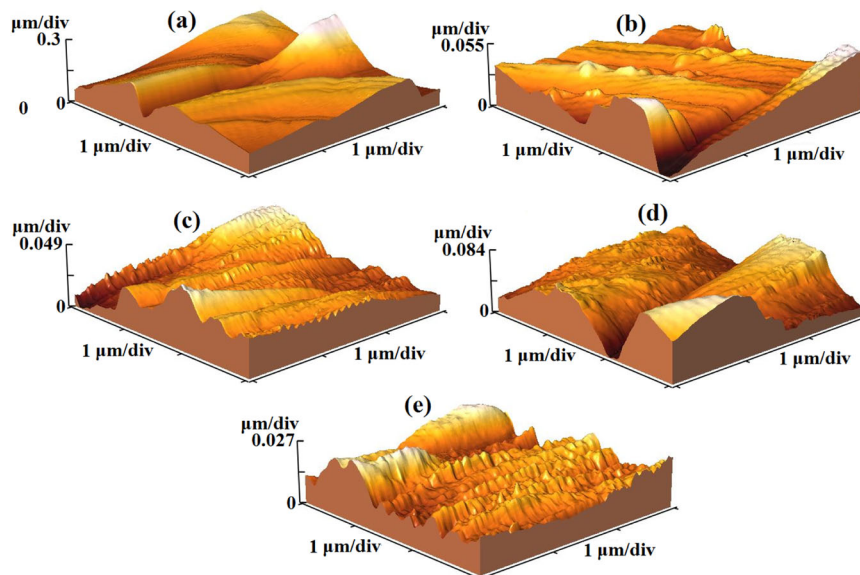


equivalent impedance plots in which the polarization resistance can be determined from $R_p = R_i + R_{ox-hyd}$.

Fig. S1 of the Supplementary Material shows the variations of R_p for the coated sample without MWCNTs and Al₂O₃. In the first stage, an increase in immersion time from

30 to 60 min partly decreased the R_p value which can be assigned to the penetration of the corrosive agents into the coating cracks as revealed in the SEM micrographs (see Figs. 2(a) and 3(a)). Prolonging the immersion time to 240 min enhanced the R_p probably due to the filling of the

Fig. 10 Topographic AFM images of (a) the pristine coating and mono-layer coatings containing (b) 0.02 wt.%, (c) 0.05 wt.%, (d) 0.1 wt.%, and (e) 0.15 wt.% MWCNTs along with 2 wt.% Al_2O_3



imperfections, cracks, and other opening pores by the corrosion products. In other words, filling the voids and cracks hindered the entrance of corrosive agents. For the immersion time of 480 min, the R_p value gradually decreased, suggesting the re-opening of the pores.

EIS plots of the double-layer coating containing 0.02 wt.% MWCNTs and 2 wt.% Al_2O_3 (see Fig. S2 in Supplementary Material for details) show a reduction in R_p by prolonging the immersion time from 30 to 60 min. Further enhancements of the immersion time up to 480 min incremented the R_p . The occupation of the cracks by MWCNTs led to thicker and denser film which prevented the penetration of corrosive solution toward the substrate; hence, incrementing R_p . A similar trend could be observed in the coating with 0.05 wt.% MWCNTs (plots are presented in Supplementary Fig. S3).

The EIS plots of the double-layer coating containing 0.1 wt.% MWCNTs reveal a substantial decline in the polarization resistance upon prolonging the immersion time from 30 to 60 min (Supplementary Fig. S4). However, a gradual increase in R_p value is a predominant trend for the exposure time of 240 min. Under such conditions, cracks and pores of the coating are filled with MWCNTs and Al_2O_3 particles, forming a dense and anti-corrosion coating.

Polarization resistance of the coating containing 0.15 wt.% MWCNTs increased by enhancing the exposure time from 30 to 120 min; whereas R_p exhibited a slight decrease by prolonging the immersion time to 480 min (Fig. S5(a)). These results indicated the higher R_p values of all compositions of double-layer coatings compared to the coating free of MWCNTs and Al_2O_3 for various immersion times. On the other hand, the R_p value of double-layer coating containing 0.15 wt.% MWCNTs was higher than other coatings (with different MWCNT concentrations) at

all immersion times. Furthermore, the application of a nanocomposite coating containing 0.15 wt.% MWCNTs and 2 wt.% Al_2O_3 strongly improved the corrosion resistance capacity of the magnesium alloy.

The EIS results were validated by the potentiodynamic polarization tests as the complementary activities on the double-layer coatings after their immersion in 3.5 wt.% NaCl solution for 2 h (Fig. 11(a)). Several data such as corrosion potential (E_{corr}), cathodic Tafel slope (B_C), and corrosion current density (J_{corr}) can be extracted from PD tests as listed in Table 1. The parameter of J_{corr} is a kinetic factor which is directly proportional to the corrosion rate of the samples. Any increase in the MWCNTs content up to 0.02 wt.% decreased the J_{corr} compared to the MWCNT- and Al_2O_3 -free sample. A rise in the concentration of MWCNTs to 0.05, 0.1, and 0.15 wt.% reduced the J_{corr} . The lowest J_{corr} was observed in the sample containing 0.15 wt.% MWCNTs. Therefore, the sample containing 0.15 wt.% MWCNT possessed the lowest corrosion rate.

EIS plots of mono-layer coatings containing 0.02 and 0.05 wt.% MWCNTs along with 2 wt.% Al_2O_3 are shown in Figs. S6, S7 in Supplementary Material for various immersion times. Nyquist plots with two time constants equivalent to the electrochemical circuit are also depicted in Supplementary Fig. S8(d). Experimental data were analyzed by the Zsim software based on the equivalent circuit whose calculated parameters are summarized in Table S2 of Supplementary Material.

EIS plot of the mono-layer coating loaded with 0.02 wt.% MWCNTs shows a continuous increase in the polarization resistance by prolonging the immersion time from 30 to 480 min such that a maximum value was observed for the immersion time of 480 min (see Fig. S6 for details). This value is higher than that of the pristine

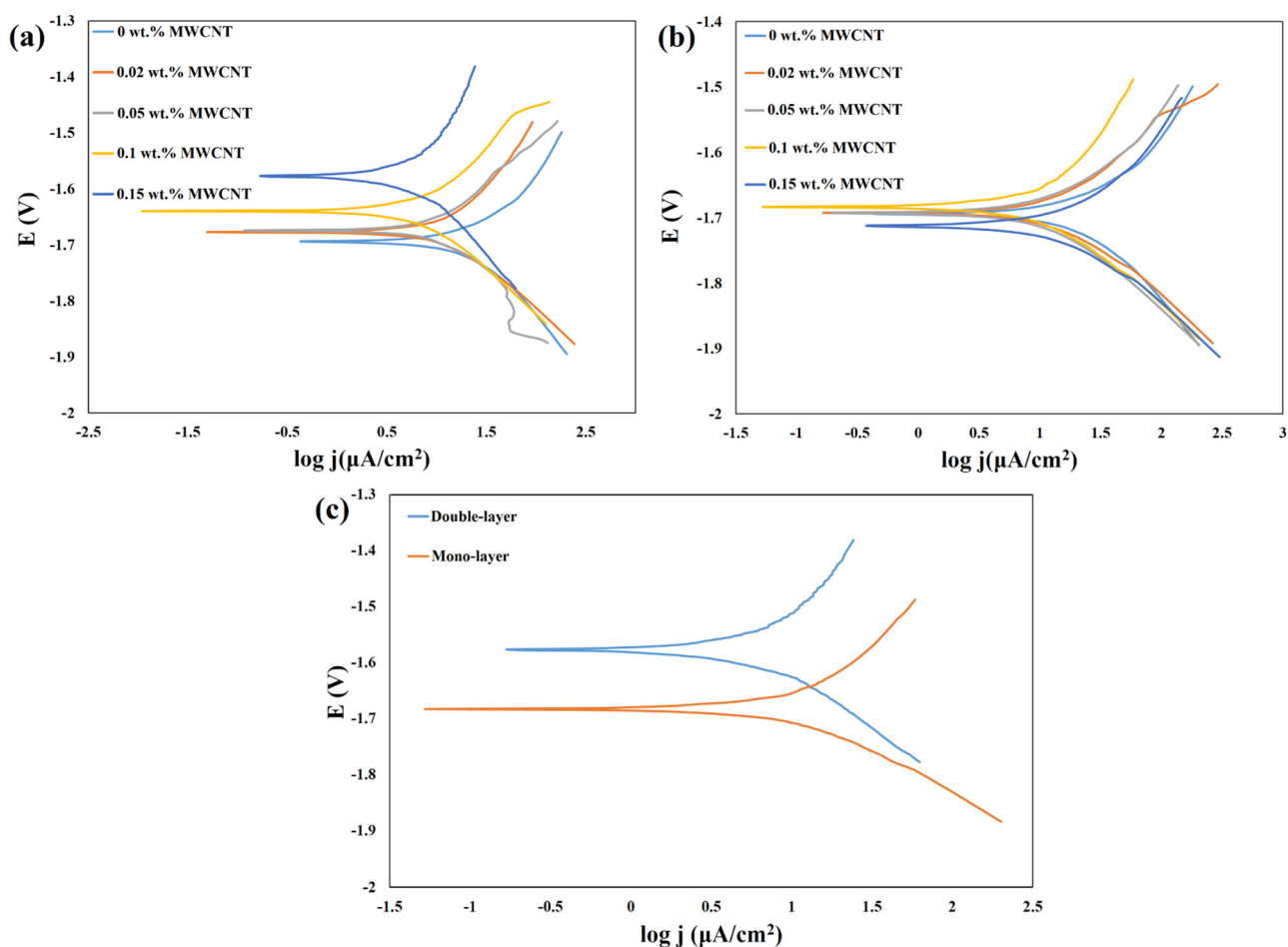


Fig. 11 Potentiodynamic polarization curves of: (a) double-layer; (b) mono-layer coatings with different MWCNT contents, and (c) mono- and double-layer coatings at their optimal MWCNT contents (0.1 and 0.15 wt.%, respectively) after 2 h of immersion in 3.5 wt.% NaCl solution

Table 1 The corrosion parameters for the double- and mono-layer coatings concluded from potentiodynamic polarization tests

MWCNT content (Wt.%)	Coatings discription	E_{Corr} (V)	B_C (mV)	J_{Corr} ($\mu\text{A}\cdot\text{cm}^{-2}$)
0	-	-1.6945	-265.8	35.049
0.02	double-layer	-1.6771	-148.7	12.583
	mono-layer	-1.6925	-190.4	23.613
0.05	double-layer	-1.6730	-128.3	8.897
	mono-layer	-1.692	-205.9	21.062
0.1	double-layer	-1.6398	-151.0	6.785
	mono-layer	-1.6833	-167.5	13.065
0.15	double-layer	-1.5783	-203.2	6.608
	mono-layer	-1.7124	-202.1	30.305

coating, suggesting the positive influence of MWCNTs on the corrosion resistance capacity of the mono-layer samples. Similarly, an increase can be detected in R_p by prolonging

the exposure time in the coating loaded with 0.05 wt.% MWCNTs (refer to Fig. S7 for more details).

Fig. S5(c–g) show the EIS plots of the mono-layer coating containing 0.1 wt.% MWCNTs and 2 wt.% Al_2O_3 , suggesting its better corrosion resistance compared to the pristine coating. The R_p value showed a drastic increase compared to the coating free of MWCNTs and Al_2O_3 particles at all immersion times. Meanwhile, the R_p value of the coating with 0.1 wt.% MWCNTs was higher than the other mono-layer coatings.

Finally, electrochemical impedance spectroscopic results of the mono-layer coating loaded with 0.15 wt.% MWCNTs are shown in Fig. S8 of the Supplementary Material. As seen, an increase in exposure time from 30 to 120 min enhanced the R_p parameter. This R_p was lower than that of the coating prepared with 0.1 wt.% MWCNTs. The positive influence of the MWCNTs appeared to stop with a further increase of the MWCNTs concentration (beyond 0.1 wt.%). Probably the coating surface cracks could not be

Table 2 The fitted quantitative parameters for bare AZ91 Mg alloy obtained from the equivalent circuit for different immersion times in the 3.5 wt.% NaCl solution

Sample	Time (min)	Q_{ct} ($\mu S^n \Omega^{-1} cm^{-2}$)	n_{ct}	R_{ct} ($k\Omega cm^2$)	Fitting error
Bare AZ91	30	7.6	0.862	1.2620	0.0199
Mg alloy	60	9.2	0.834	0.8021	0.0239
	120	9.1	0.855	0.8291	0.0282
	240	9.4	0.800	0.7357	0.0283
	480	16.1	0.782	0.6581	0.0389

appropriately filled due to aggregation and agglomeration of MWCNTs, resulting in lower R_p levels.

After careful studies of EIS curves concerning the AZ91 alloy covered with mono- and double-layer silane coating containing MWCNTs and Al_2O_3 particles, it is better to provide the impedance response for a bare Mg alloy substrate to evaluate the protective performance of the mono- and double-layer coatings. Fig. S9 of the Supplementary Material shows the Nyquist (a), Bode modulus (b), phase Bode plots (c), and corresponding equivalent circuit (d) of the bare AZ91 alloy tested in the 3.5 wt.% NaCl solution at different immersion times. As can be seen, the bare AZ91 alloy exhibits single capacitive semicircle which can be attributed to resistance of AZ91 magnesium alloy based on equivalent circuit. It has very low resistance in comparison with coated samples, indicating its weak corrosion resistance. Additionally, the fitted quantitative parameters of bare AZ91 Mg alloy were extracted based on equivalent circuit as listed in Table 2.

Fig. 11(b) presents the potentiodynamic polarization curves of the mono-layer coating with different MWCNT contents immersed in 3.5 wt.% NaCl solution for 2 h.

The incorporation of MWCNTs into mono-layer coatings up to 0.1 wt.% decreased the J_{corr} compared to the coated sample free of MWCNTs and Al_2O_3 . The sample loaded with 0.15 wt.% MWCNTs, however, showed higher J_{corr} . Other corrosion parameters can be found in Table 1. The PD results also confirmed the EIS fitting data of the mono-layer coatings.

Despite some erratic variations in Q_i and Q_{ox-hyd} values, these parameters show a gradual increase with prolonging the immersion time (see Tables S1 and S2 of the Supplementary Material). Water has a high dielectric constant; thus, its penetration into sol-gel film increases the capacitive values. The mono- and double-layer coatings containing 0.1 and 0.15 wt.% MWCNTs showed the lower capacitive values at all immersion times, confirming the corrosion resistance capacities of the coatings.

According to the above discussions, the optimum MWCNT concentration for the best corrosion resistance is 0.15 wt.% for the double-layer coatings of MWCNT/ SiO_2 + Al_2O_3 ; whereas, 0.1 wt.% MWCNTs is the optimal

concentration in the case of mono-layer coating. Concerning the surface cracking of the coatings, the optimum concentration of MWCNTs is 0.15 and 0.1 wt.% for double- and mono-layer MWCNT/ SiO_2 + Al_2O_3 coatings, respectively. The results of the FE-SEM micrographs and the EIS analysis are in good agreement with those of the optimum MWCNT concentrations in terms of the cracking and corrosion resistance.

The polarization resistances of the double- and mono-layer coatings with optimal MWCNTs concentrations were respectively 349.6 and 183.4 $k\Omega cm^2$ for the immersion time of 120 min. Furthermore, the EIS results suggest that the protection ability of optimal double-layer coating is partly higher than that of the optimal mono-layer coating. On the other hand, the PD results of the mono- and double-layer coatings with optimal MWCNTs content (Fig. 11(c)) indicated the lower corrosion current density and positive corrosion potential of the double-layer coating containing 0.15 wt.% MWCNTs, suggesting its slow corrosion rate.

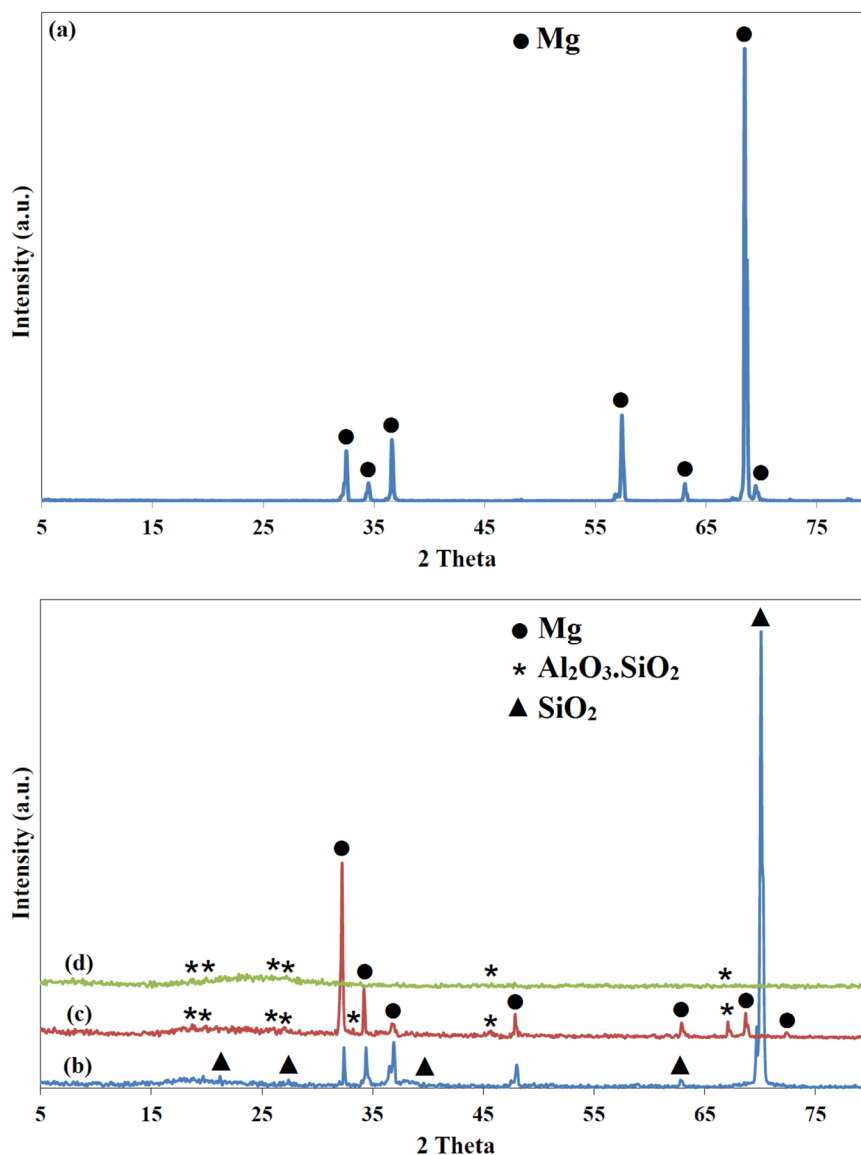
The two-layer coating exhibited higher corrosion resistance than mono-layer coating. It is an expected result, as the two-layer system has a higher thickness. In this situation, the effect of alumina as a processing parameter can be neglected on the corrosion resistance of the developed coating. In other words, the better performance of the two-layer sample may be only due to its higher thickness, and the significant effect of alumina presence on corrosion resistance may be hidden. To remove such an ambiguity, two samples with similar thickness were prepared with and without alumina, and their protective performances were compared. Fig. S10 shows the EIS results of the double-layer coatings of similar thicknesses with/without alumina additive loaded with 0.1 wt.% MWCNTs after 480 min of immersion. The R_p value of the alumina-containing coating showed an increase (152.3 $k\Omega cm^2$) compared to the Al_2O_3 -free coating (128.4 $k\Omega cm^2$); confirming the positive effect of Al_2O_3 on the corrosion performance of the coating.

The discrepancy with other methods [28] can be ascribed to the incorporation of alumina filler on the corrosion resistance of the proposed coating. EIS analysis confirmed the positive effect of Al_2O_3 addition on the corrosion performance of the coating, highlighting the unique effect of the proposed coating system compared to similar coatings [28]. Furthermore, a double-layer coating system with 0.15 wt.% MWCNTs and alumina additive can be proposed as a promising candidate to protect AZ91 magnesium alloy against corrosion with superior features compared to other samples which is the main contribution of this research.

3.4 XRD studies

Fig. 12 shows the XRD patterns of the samples prepared under various conditions. The XRD spectra of the bare AZ91 magnesium alloy are depicted in Fig. 12(a). Figure 12(b) shows to

Fig. 12 The XRD patterns of: (a) bare AZ91 magnesium alloy, (b) pristine silane coating with no MWCNTs and Al_2O_3 , (c) double-layer coating prepared with MWCNT and alumina, and (d) silane nanocomposite with MWCNTs and Al_2O_3 without substrate



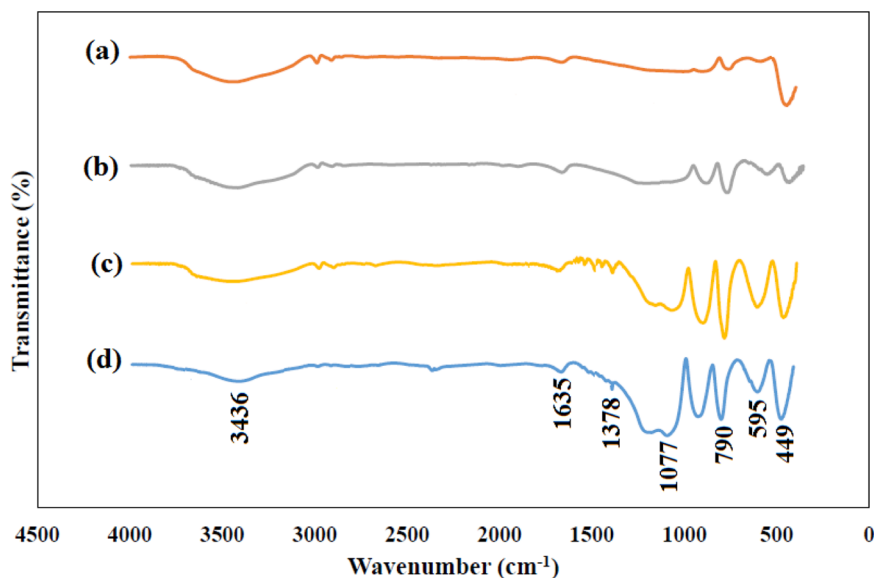
the XRD pattern of pristine silane coating with no MWCNTs and Al_2O_3 where, the peaks of Mg and SiO_2 can solely be observed. XRD pattern of Fig. 12(c) refers to the double-layer coating with MWCNT and alumina additive. The aluminum silicate ($\text{Al}_2\text{O}_3\cdot\text{SiO}_2$) phase along with base metal of substrate could be detected in the mentioned sample, whereas, the MWCNTs peaks could not be observed due to their insignificant concentration. The last spectrum is attributed to silane nanocomposite with MWCNTs and Al_2O_3 additive and no substrate (Fig. 12(d)). This specimen exhibited lower crystallinity. This figure depicts weak peaks of aluminum silicate along with slight SiO_2 phase but no peaks related to MWCNTs.

3.5 Fourier Transformation Infrared Spectroscopy

Fig. 13(a–b) depict the FTIR spectra of the coatings (without substrate) containing 0.15 wt.% MWCNTs prepared under

different conditions. The broad band at $3000\text{--}3700\text{ cm}^{-1}$ and a small peak at $\sim 1635\text{ cm}^{-1}$ can be attributed to the O-H stretching vibration of insufficient silanol group (Si-OH) condensation along with some residual absorbed water [34–36]. The mentioned peak loses its intensity by increasing the drying temperature due to the evaporation and removal of the hydroxyl group, such that it somewhat attenuates in the dried sample at 130°C . The band at 450 cm^{-1} can be ascribed to the bending vibrations of O-Si-O linkage [37] whereas, the peaks at 1077 and 790 cm^{-1} belong to the asymmetric and symmetric stretching vibrations of Si-O-Si bridges [34–37]. These peaks got stronger by increasing the drying temperature due to the successful condensation reaction between Si-OR groups. In the spectrum of the samples (c) and (d), the absorption peaks at 595 and 1378 cm^{-1} can be attributed to the Al-O stretching vibration in octahedral structure [38]. Additionally, a symmetric bending mode belonging to the

Fig. 13 the FTIR spectra of (a) silica gel; (b) SiO₂/MWCNT gel; (c) SiO₂ + Al₂O₃/MWCNT gel dried at room temperature and (d) SiO₂ + Al₂O₃/MWCNT gel dried at 130 °C for 2 h



Al-O-H structure can be detected at 1072 cm⁻¹ [38]; which is not clear due to overlapping with the Si-O-Si vibration. Finally, two peaks at 1205 and 1580 cm⁻¹ can be assigned to the carbon skeleton and the presence of the cylinder-like carbon structure [39, 40] which could not be distinguished probably due to low MWCNT concentration and overlapping of the bands.

4 Conclusion

The corrosion behavior of a magnesium alloy (AZ91) coated by mono- and double-layers of silane-Al₂O₃/MWCNT sol-gel nanocomposite was investigated in this study. The main conclusions are listed as follows:

- (1) The minimum number of cracks was observed in the mono-layer coatings prepared by 0.1 wt.% MWCNTs; while the minimum crack of the double-layer coatings was observed in the samples loaded with 0.15 wt.% MWCNTs.
- (2) The average roughness of the double-layer coatings was reduced by enhancing the MWCNT content. For mono-layer coatings, this parameter increased up to the MWCNT content of 0.1 wt.% followed by a decrement.
- (3) Based on EIS and PD results, the maximum polarization resistance and minimum corrosion current density of the mono and double-layer coatings were observed in the samples containing 0.1 and 0.15 wt.% MWCNTs, respectively.
- (4) The protection performance of double-layer coating was partly higher than that of mono-layer coating in their optimal MWCNT concentrations; hence, applying a double layer coating with 0.15 wt.% MWCNTs along

with 2 wt.% alumina could more effectively protect the AZ91 magnesium alloy.

Supplementary information The online version contains supplementary material available at <https://doi.org/10.1007/s10971-023-06181-z>.

References

1. Rajabalizadeh Z, Seifzadeh D, Habibi-Yangjeh A, Mesri Gundoshmian T, Nezamdoust S (2018) Electrochemical noise analysis to examine the corrosion behavior of Ni–P deposit on AM60B alloy plated by Zr pretreatment. *Surf. Coat. Tech.* 346:29–39
2. Xian W, Linxin L, Xie Z-H, Yu G (2018) Duplex coating combining layered double hydroxide and 8-quinolinol layers on Mg Alloy for corrosion protection. *Electrochim. Acta* 283:1845–1857
3. Ai-hui LIU, Ji-lin XU (2018) Preparation and corrosion resistance of superhydrophobic coatings on AZ31 magnesium alloy. *T. Nonferr. Metal. Soc.* 28:2287–2293
4. Ashraf MA, Liu ZH, Peng WX, Yoysefi N (2019) Amino acid and TiO₂ nanoparticles mixture inserted into sol-gel coatings: an efficient corrosion protection system for AZ91 magnesium alloy. *Prog. Org. Coat.* 136:105296
5. Ashassi-Sorkhabi H, Moradi-Alavian S, Esrafil MD, Kazempour A (2019) Hybrid sol-gel coatings based on silanes-amino acids for corrosion protection of AZ91 magnesium alloy: electrochemical and DFT insights. *Prog. Org. Coat.* 131:191–202
6. Nezamdoust S, Seifzadeh D, Habibi-Yangjeh A (2020) Nano-diamond incorporated sol-gel coating for corrosion protection of magnesium alloy. *T. Nonferr. Metal. Soc.* 30:1535–1549
7. Talha M, Wang Q, Ma Y, Lin Y (2023) Self-assembled hybrid silane/ZnO coatings for corrosion protection of resorbable magnesium alloy. *Int. J. Adhes. Adhes.* 120:103281
8. Pereira GS, Ramirez OMP, Avila PRT, Avila JA, Pinto HC, Miyazaki MH, de Melo HG, Filho WWB (2022) Cerium

- conversion coating and sol-gel coating for corrosion protection of the WE43 Mg alloy. *Corr. Sci.* 206:110527
9. Khosravi H S, Veerapandian VK, Vallant R, Reichmann K (2020) Effect of processing conditions on the structural properties and corrosion behavior of TiO₂-SiO₂ multilayer coatings derived via the sol-gel method. *Ceram. Int.* 46:17741–17751
 10. Mohammadi I, Shahrabi T, Mahdavian M, Izadi M (2022) A novel corrosion inhibitive system comprising Zn-Al LDH and hybrid sol-gel silane nanocomposite coating for AA2024-T3. *J. Alloy Compd.* 909:164755
 11. Balaji J, Roh SH, Edison TNJI, Jung HY, Sethuraman MG (2020) Sol-gel based hybrid silane coating for enhanced corrosion protection of copper in aqueous sodium chloride. *J. Mol. Liq.* 302:112551
 12. Liang Y, Liu B, Zhang B, Liu ZH, Liu W (2021) Effects and mechanism of filler surface coating strategy on thermal conductivity of composites: A case study on epoxy/SiO₂-coated BN composites. *Int. J. Heat Mass Tran.* 164:120533
 13. Poelman M, Fedel M, Motte C, Lahema D, Th. Urios, Paint Y, Deflorian F, Olivier MG (2015) Influence of formulation and application parameters on the performances of a sol-gel/clay nanocomposite on the corrosion resistance of hot-dip galvanized steel. Part I. Study of the sol preparation parameters. *Surf. Coat. Tech.* 274:1–8
 14. Ansari F, Naderi R, Dehghanian C (2015) Study on the protective function of cloisite incorporated silane sol-gel coatings cured at different conditions. *Appl. Clay Sci.* 114:93–102
 15. Both J, Szabo G, Katona G, Muresan LM (2022) Tannic acid reinforced sol-gel silica coatings for corrosion protection of zinc substrates. *Mat. Chem. Phys.* 282:125912
 16. Shi Y, Yuan SH, Ter-Ovanesian B, Hermange K, Huo Y, Normand B (2021) Enhancing the barrier effect of sol-gel derived inorganic coating by doping h-BN nanosheet. *Appl. Surf. Sci.* 544:148849
 17. Yang M, Wang T, Wu M (2021) Ablation behavior of SiC whisker and ZrB₂ particle-filled ZrO₂ sol-gel composite coating under high-intensity continuous laser irradiation. *Ceram. Int.* 47:26327–26334
 18. Fernandez-Hernan JP, Torres B, Lopez AJ, Martinez-Campos E, Rams J (2021) Sol-gel coatings doped with graphene nanoplatelets for improving the degradation rate and the cytocompatibility of AZ31 alloy for biomedical applications. *Surf. Coat. Tech.* 426:127745
 19. Seifzadeh D, Golmoghani-Ebrahimi E (2012) Formation of novel and crack free nanocomposites based on sol gel process for corrosion protection of copper. *Surf. Coat. Tech.* 210:103–112
 20. Suleiman RK, Kumar AM, Rahman MM, Al-Badour FA, Meliani MH, Saleh TA (2020) Effect of metal oxide additives on the structural and barrier properties of a hybrid organosilicon sol-gel coating in 3.5% NaCl medium. *Prog. Org. Coat.* 148:105825
 21. Liu Y, Lin Q, Chen J, Shao Y, Wang Y, Wang J (2022) PDMS-OH and nano-SiO₂ Modified KH570-TEOS silica-sol coating and protective effect on concrete. *Colloid Surface A* 648:129279
 22. Parhizkar N, Ramezanzadeh B, Shahrabi T (2018) Corrosion protection and adhesion properties of the epoxy coating applied on the steel substrate pre-treated by a sol-gel based silane coating filled with amino and isocyanate silane functionalized graphene oxide nanosheets. *Appl. Surf. Sci.* 439:45–59
 23. Liu Y, Cao H, Yu Y, Chen SH (2015) Corrosion protection of silane coatings modified by carbon nanotubes on stainless steel. *Int. J. Electrochem. Sci.* 10:3497–3509
 24. Karbasi M, Yazdian N, Vahidian A (2012) Development of electro-co-deposited Ni-TiC nano-particle reinforced nanocomposite coatings. *Surf. Coat. Tech.* 207:587–593
 25. Jiang L, Han M, Sun J, Gong M, Lin Y, Xiao T, Xiang P, Chen W, Tan X (2023) Strong mechanical and durable superhydrophobic photothermal MWCNTs/SiO₂/PDMS/PVDF composite coating for anti-icing and de-icing. *Prog. Org. Coat.* 174:107282
 26. Song R, Zhang SH, He Y, Li H, Fan Y, He T, Zhang Y, Xiang Y, Zhang H (2021) Effect of H-MWCNTs addition on anti-corrosion performance and mechanical character of Ni-Cu/H-MWCNTs composite coatings prepared by pulse electrodeposition technique. *Colloid Surface A* 630:127519
 27. Wei J, Sun L, Han J, Huang W (2022) MWCNTs/CB waterborne conductive smart coating for damage monitoring of composites: Design, fabrication, characterization, and verification. *Prog. Org. Coat.* 172:107136
 28. Nezamdoust S, Seifzadeh D, Rajabalizadeh Z (2018) PTMS/OH-MWCNT sol-gel nanocomposite for corrosion protection of magnesium alloy. *Surf. Coat. Tech.* 335:228–240
 29. Lopez AJ, Urena A, Rams J (2010) Fabrication of novel sol-gel silica coatings reinforced with multi-walled carbon nanotubes. *Mater. Lett.* 64:924–927
 30. Fernandez-Hernan JP, Lopez AJ, Torres B, Rams J (2020) Silicon oxide multilayer coatings doped with carbon nanotubes and graphene nanoplatelets for corrosion protection of AZ31B magnesium alloy. *Prog. Org. Coat.* 148:105836
 31. Daavari M, Atapour M, Mohedano M, Sanchez HM, Rodriguez-Hernandez J, Matykina E, Arrabal R, Taherizadeh A (2022) Quasi-in vivo corrosion behavior of AZ31B Mg alloy with hybrid MWCNTs-PEO/PCL based coatings. *J. Magnes. Alloy* 10:3217–3233
 32. Jia J, Zhang B, Liu D, Liu SH, Ji G, Ji R (2020) Effects of Al₂O₃ coating induced structural and mechanical changes of C/C composites. *J. Alloy compd.* 818:152847
 33. Mohammadi I, Shahrabi T, Mahdavian M, Izadi M (2021) Zn-Al layered double hydroxide as an inhibitive conversion coating developed on AA2024-T3 by one-step hydrothermal crystallization: Crystal structure evolution and corrosion protection performance. *Surf. Coat. Tech.* 409:126882
 34. Nallamuthu N, Prakash I, Venkateswarlu M, Balasubramanyam S, Satyanarayana N (2008) Sol-gel synthesis and characterization of Li₂O-As₂O₅-SiO₂ glassy System. *Mat. Chem. Phys.* 111:24–28
 35. Tran ThN, Pham ThVA, Le MLPh, Nguyen ThPhTh, Tran VM (2013) Synthesis of amorphous silica and sulfonic acid functionalized silica used as reinforced phase for polymer electrolyte membrane. *Adv. Nat. Sci.: Nanosci. Nanotechnol* 4:045007
 36. Boulesbaa M (2021) Spectroscopic ellipsometry and FTIR characterization of annealed SiO_xN_y:H films prepared by PECVD. *Opt. Mater.* 122:111693
 37. Kazancioglu M, Tsilomelekis G, Lehman R, Hara M (2021) FTIR studies on plasticization of silicate glass with ionic liquids (conversion to silicate polymers). *J. Non-Cryst. Solids* 561:120757
 38. Djebaili K, Mekhalif Z, Boumaza A, Djelloul A (2015) XPS, FTIR, EDX, and XRD analysis of Al₂O₃ scales grown on PM2000 alloy. *J. Spectrosc.* 2015:868109
 39. Li Y, Xu C, Wei B, Zhang X, Zheng M, Wu D, Ajayan PM (2002) Self-organized ribbons of aligned carbon nanotubes. *Chem. Mater.* 14:483–485
 40. Afghahi SSS, Peymanfar R, Javanshir SH, Atassi Y, Jafarian M (2017) Synthesis, characterization and microwave characteristics of ternary nanocomposite of MWCNTs/doped Sr-hexaferrite/PANI. *J. Magn. Magn. Mater.* 423:152–157

Publisher's note Springer Nature remains neutral with regard to jurisdictional claims in published maps and institutional affiliations.

Springer Nature or its licensor (e.g. a society or other partner) holds exclusive rights to this article under a publishing agreement with the author(s) or other rightsholder(s); author self-archiving of the accepted manuscript version of this article is solely governed by the terms of such publishing agreement and applicable law.